12th International Symposium on Turbulence and Shear Flow Phenomena (TSFP12)
Osaka, Japan (Online), July 19-22, 2022

TURBULENT MEAN FLOW ESTIMATION WITH STATE OBSERVER ASSIMILATION OF VELOCITY MEASUREMENTS IN RANS MODELS

Olivier Marquet, Vincent Mons, Markus Zauner and Benjamin Leclaire
DAAA
ONERA, Université Paris Saclay
8 rue des Vertugadins, 92190 Meudon, France
olivier.marquet@onera.fr

INTRODUCTION

The full characterization of complex turbulent flows is a challenging task in industrial applications. On the one hand, scale-resolving computational fluid dynamics approaches, such as Direct Numerical Simulations (DNS) or Large Eddy Simulations (LES), allow accurate estimation of time-averaged and fluctuating quantities but they become very expensive for flows with increasing Reynolds numbers. Therefore, small-scale structures are often not fully resolved but modeled, which raises the issue of fidelity. On the other hand, experimental techniques may provide accurate information about the full complexity of flows of interest. However, spatial and temporal resolution of measurements is often sparse and/or limited to certain quantities, while boundary or freestream conditions are often hard to characterize precisely.

Data assimilation techniques (Hayase, 2015) are increasingly considered to overcome the above-mentioned respective limitations, combining advantages of numerical and experimental approaches. It aims at merging experimental and numerical results in order to compensate for model and parameter uncertainties in numerical simulations on the one hand, and to provide a full flow estimation from limited experimental data on the other hand. The outcome of data assimilation is thus an augmented flow prediction that combines the fidelity of the experimental/reference data and the comprehensive description that is offered by numerical simulation.

State-of-the-art data assimilation techniques include variational approaches, which rely on adjoint models to minimize discrepancies between measurements and numerical flow estimation, and Kalman filter-based methodologies, which are derived from a Bayesian formulation of data assimilation. While these two types of techniques may benefit from strong mathematical foundations, their application requires large computational costs, which may be of the order of one hundred baseline simulations. The costs of variational approaches are mainly driven by the number of optimization iterations to ensure convergence (Yegavian *et al.*, 2015), while the computational requirements of Kalman filters are due to the need of propagating uncertainties in the flow state estimation, possibly through Monte-Carlo techniques (Mons *et al.*, 2016). In any case, the above-mentioned computation cost may hinder the application of these data-assimilation techniques for complex flows.

In the present contribution, we study the use of an alternative and possibly over-looked data assimilation approach, namely nudging (Lakshmivarahan & Lewis, 2013), which may also be referred to as state observer in the literature (Hayase, 2015). It consists in adding a forcing term to the governing flow equations that is proportional to the difference between reference data and numerical prediction. As such, the assimilation of data with state observer techniques is straightforward to implement and virtually induces no supplementary cost compared to a baseline simulation. It has recently regained interest in numerical (Zerfas *et al.*, 2019) and experimental fluid mechanics (Saredi *et al.*, 2021) due to its good performances in state estimation from limited data, in particular in the case of fundamental turbulent flows (Di Leoni *et al.*, 2020).

In the present study, we are interested by improving the estimation of turbulent mean-flows as modeled with Reynolds Averaged Navier-Stokes (RANS) equations thanks to the assimilation of sparse pointwise velocity. This objective was recently addressed by Zauner *et al.* (2022) for the mean-flow velocity around a square cylinder at the diameter-based Reynolds number $Re = 22000$. Results of direct numerical simulations exhibit broad-band high-frequency Kelvin-Helmholtz fluctuations in the shear layers that emerge at the leading-edge corners of the square cylinder, as well as low-frequency quasi-periodic vortex shedding in its wake. Simulations based on the Unsteady Reynolds Averaged Navier-Stokes equations (URANS), such as those performed with the turbulent Spalart-Allmaras model (Spalart & Allmaras, 1994), predict low-frequency periodic-oscillation of the wake but fail to capture the high-frequency fluctuations (Iaccarino *et al.*, 2003). Recently, Zauner *et al.* (2022) have shown that the assimilation of spanwise- and time-averaged pointwise velocity data (which were extracted from DNS) into an URANS model allows to improve the low-frequency prediction but also to capture the high-frequency fluctuations of the shear layers. As for a wide range of aerospace applications mean-flow estimates are often sufficient, we here investigate the state-observer assimilation of pointwise velocities into a steady RANS model. Besides the fact that solving such a steady model is more computationaly efficient than its unsteady counterpart, the state-observer assimilation technique only requires time-independent and average pointwise velocity data. One of the difficulty raised by the assimilation of pointwise velocity data is the appearance of spurious flow oscillations around the measurement locations, as observed by Zauner *et al.* (2022) in the framework of unsteady data-assimilation. Following Azouani *et al.* (2014); Zerfas *et al.* (2019); Rebholz & Zerfas (2021), they used an interpolant-based approach to reduce that detrimental effect on the unsteady flow estimation. We thus here propose to investigate this interpolant-based approach in the present context of assimilation of time-averaged pointwise velocities based on RANS.

The manuscript is organized in two parts. Section 1 describes the flow configuration, the numerical methods and the results of standard RANS models. Section 2 is dedicated to the state-observer assimilation method and its application to the turbulent flow estimation around a square cylinder. The pointwise- and interpolant-based approaches are first exposed, the influences of the choice of the nudging coefficient and distance between measurements are then investigated, before concluding with a comparison between steady and unsteady data assimilation.

1 TURBULENT FLOW PREDICTION WITH THE STANDARD MODEL

We investigate the turbulent flow around a square cylinder at Reynolds number $Re = U_\infty D/\nu = 22000$, where ν is the kinematic viscosity, U_∞ is the upstream uniform velocity and D is the cylinder's diameter. The origin of the cartesian coordinate system (x,y) is located at the center of the cylinder. Hereinafter, all the spatial coordinates and flow variables are made non-dimensional using D as length scale, U_∞ as velocity scale, and ρD^2 as mass scale (per unit length), where ρ is the fluid density.

Three-dimensional Direct Numerical Simulation (DNS) of the flow, that is turbulent in the wake of the square cylinder, were performed by Dandois *et al.* (2018) with ONERA's FastS solver. The unsteady flow variables were spanwise- and time-averaged to generate the two-dimensional mean-flow velocity $\mathbf{u}_r$, which is shown in figure 1(a). It is used not only as a reference mean-flow but also to generate synthetic pointwise observations, as detailed later. The iso-contours of the streamwise velocity, displayed in the figure, clearly indicate the existence of a short symmetric recirculation region downstream the square cylinder, that extends up to $x = 0.95$. A computationally efficient way to estimate this mean-flow is to solve the following two-dimensional Reynolds-Averaged-Navier-Stokes equations

$$(\mathbf{u}\cdot\nabla)\mathbf{u} + \nabla p - \nabla\cdot\left[2\left(\frac{1}{Re} + \nu_t(\tilde{\nu})\right)\mathbf{S}(\mathbf{u})\right] = \mathbf{0} \qquad (1)$$
$$\nabla\cdot\mathbf{u} = 0,$$

where $\mathbf{u} = (u,v)$ and p denote the mean velocity vector and pressure, respectively. To obtain the above equations, the Boussinesq assumption has been used to express the Reynolds stress tensor as a function of $\mathbf{S}(\mathbf{u})$, denoting the strain-rate tensor of the mean velocity. The (non-dimensional) eddy-viscosity field ν_t is thus introduced in the momentum equations. In the present study, it depends on the variable $\tilde{\nu}$ satisfying the following Spalart-Allmaras equation

$$(\mathbf{u}\cdot\nabla)\tilde{\nu} = s(\tilde{\nu},\mathbf{u}), \qquad (2)$$

where s refers to the source, diffusion and dissipation terms (Spalart & Allmaras, 1994).

For this convection-dominated flow, the Streamline Upwind Petrov Galerkin (SUPG) finite-element method (Brooks & Hughes, 1982) is used to discretize the standard RANS equations (1) and (2). The rectangular computational domain is defined in $-10 \le x \le 15$ and $-10 \le y \le 10$. An anisotropic mesh adaptation based on the reference mean velocity and pressure (Fabre *et al.*, 2018) is performed to obtain the mesh made of triangles for a total of $\sim 5\cdot 10^4$ vertices that is used hereinafter. The discretized non-linear equations, obtained using the FreeFEM open-source software (Hecht, 2012), are then solved using a quasi Newton method. At the k^{th} iteration of this algorithm, a linearized problem around the current solution $(\mathbf{u}^k, p^k, \tilde{\nu}^k)$ is solved with a direct LU solver, yielding the correction $(\delta\mathbf{u}^k, \delta p^k, \delta\tilde{\nu}^k)$. The solution is then updated as $(\mathbf{u}^{k+1}, p^{k+1}, \tilde{\nu}^{k+1}) + \gamma^k(\delta\mathbf{u}^k, \delta p^k, \delta\tilde{\nu}^k)$, where the coefficient γ^k is progressively increased with the number of iterations, unlike for the Newton method where it is kept fixed to $\gamma = 1$. This quasi-Newton method is crucial to avoid divergence of the algorithm, especially when considering the nudging approach described in the next section. At the inlet, the boundary condition $(u,v,\tilde{\nu}) = (1,0,0)$ is imposed. At the cylinder surface, the no-slip boundary condition $\mathbf{u} = \mathbf{0}$ is enforced in conjunction with $\tilde{\nu} = 0$. The conditions $\frac{\partial\tilde{\nu}}{\partial x} = 0$ and $2(Re^{-1} + \nu_t)\mathbf{S}(\mathbf{u})\cdot\mathbf{n} - p\mathbf{n} = \mathbf{0}$ are used at the outlet, where $\mathbf{n}$ denotes the normal vector. At the top and bottom boundaries, symmetry conditions are imposed according to $(\frac{\partial u}{\partial y}, v, \frac{\partial\tilde{\nu}}{\partial y}) = \mathbf{0}$.

Figure 1(b) displays isocontours of the streamwise mean-flow velocity obtained by solving the RANS equations (1) with the Spalart-Allmaras turbulent model (2). A symmetric recirculation region is also obtained in the wake of the square cylinder, but of much larger extent (up to $x = 3.90$) compared to the reference mean-flow (up to (up to $x = 0.96$, see figure 6-b). The absolute value of the discrepancy between the two velocity fields is depicted in figure 1(c). The large error in the wake is in agreement with the over-predicted extent of the recirculation region and can be explained by insufficient dissipation in the Spalart-Allmaras turbulence model. The objective of the present study is to improve the estimation of the mean-flow based on the SA-RANS model using state observer data assimilation and synthetic sparse measurements of the reference mean-flow, as described in the next section.

2 TURBULENT FLOW ESTIMATION WITH STATE OBSERVER ASSIMILATION OF POINTWISE VELOCITY

To improve the estimation of the turbulent mean flow based on the RANS equations, a state observer technique is investigated for the assimilation of pointwise velocity measurements of the reference mean flow $\mathbf{u}_r$.

The two components of the velocity fields are extracted as a set of M discrete points $(\mathbf{x}_i)_{i=1\cdots M}$. As shown in figure 2(a), they are here equally spaced in a measurement domain denoted Ω_m that will be specified later. The distance between those measurements is denoted d. The data vector $\mathbf{m}$, which gathers these pointwise velocity measurements is formally defined as

$$\mathbf{m} = \mathscr{H}(\mathbf{u}_r), \qquad (3)$$

where $\mathscr{H}$ is the so-called measurement operator. Unlike other data-assimilation method relying on optimization techniques, the velocity data vector is directly injected into the momentum equations (1), yielding

$$(\mathbf{u}_\gamma\cdot\nabla)\mathbf{u}_\gamma + \nabla p_\gamma - \nabla\cdot\left[2\left(\frac{1}{Re} + \nu_t(\tilde{\nu})\right)\mathbf{S}(\mathbf{u}_\gamma)\right]$$
$$= \gamma\mathscr{I}[\mathbf{m} - \mathscr{H}(\mathbf{u}_\gamma)], \qquad (4)$$

where $\mathbf{u}_\gamma$ and p_γ denote the reconstructed velocity and pressure fields. The right-hand-side term is a source term proportional to the error between the measurement of the velocity

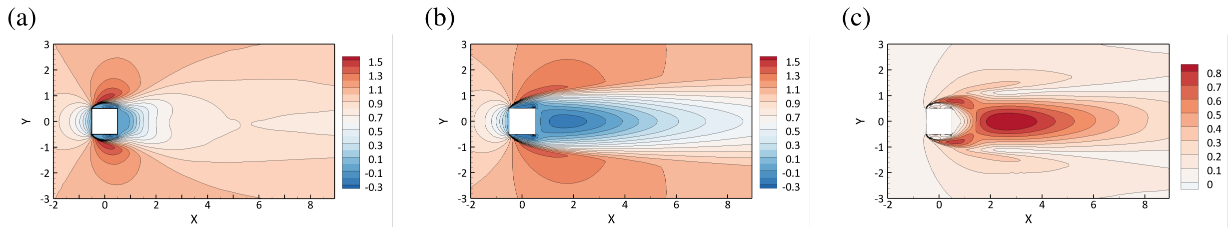

Figure 1: Streamwise velocity of (a) the spanwise- and time-averaged flow obtained from Direct Numerical Simulations (DNS) and (b) the mean-flow computed as solution of the standard Reynolds Averaged Navier-Stokes (RANS) equations using the turbulent Sparlat-Allamaras model. (c) Magnitude of the discrepancies between the DNS and RANS mean-velocity fields.

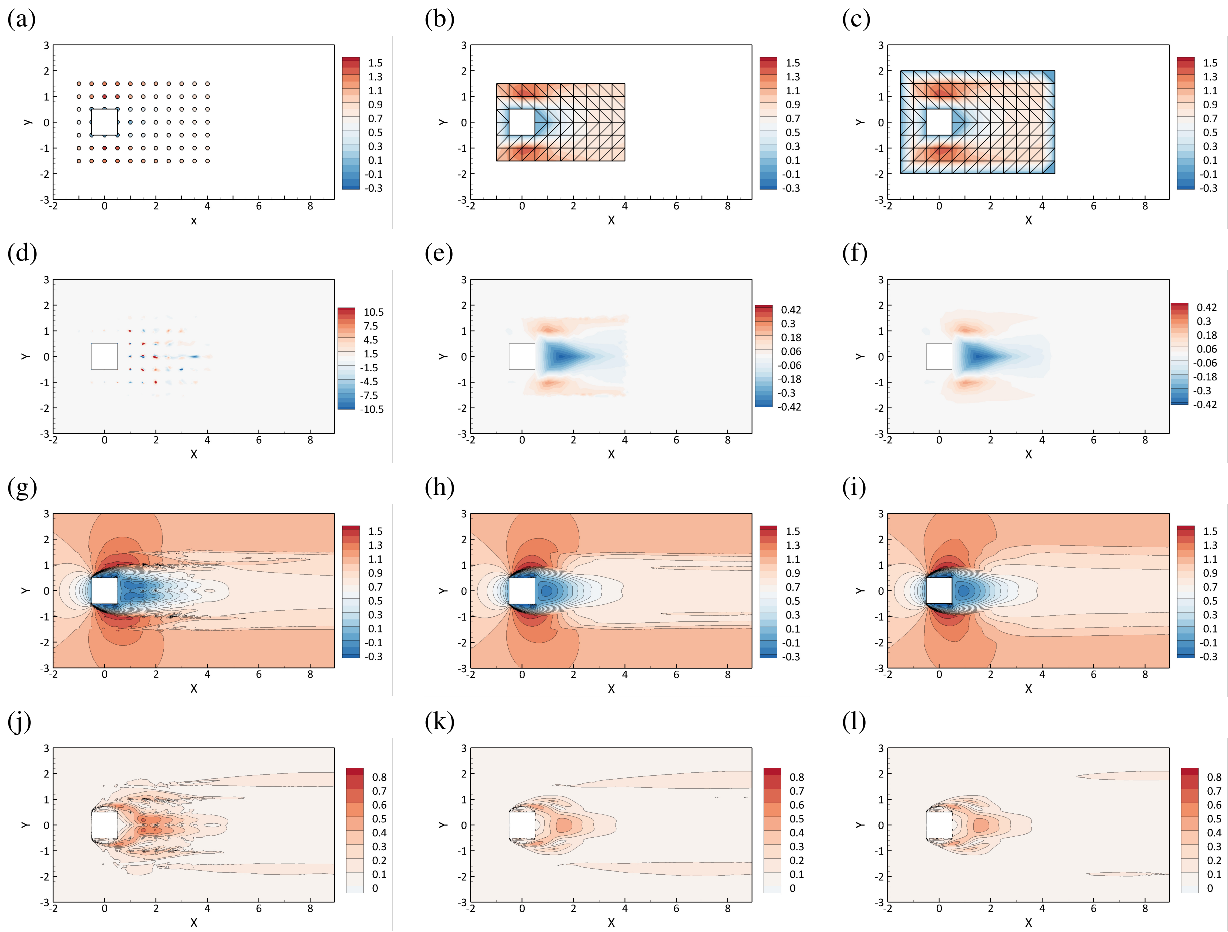

Figure 2: (a) Punctual measurements. (b,c) Linear interpolation of the measurements in (a) on two symmetric triangular meshes. Note that a layer is added to the mesh shown (c) but the values corresponding to the external nodes are set to zero, allowing a smoother interpolation at the boundaries of the measurement domain. Second, third and fourth rows correspond to the forcing $\mathscr{I}[\mathbf{m}-\mathscr{H}(\mathbf{u}_\gamma)]$ in (4), the streamwise velocity of the reconstructed solution, and corresponding error velocity field with respect to the reference (DNS) solution, respectively, using the punctual measurements shown in (a) (first column), or the linear interpolation shown in (b,c) (second and third columns).

field estimated with the RANS model and the data vector. The coefficient γ allows to vary the magnitude of this source term, while the operator $\mathscr{I}$ is introduced to map the pointwise error to the space of velocity estimated by the RANS model. Various choices for this operator are investigated in the present study.

The first one is the dual measurement operator, i.e. $\mathscr{I}=\mathscr{H}^\dagger$. In that case, the forcing in the momentum equations is localized around the measurement points, as shown in figure 2(d). Such forcing may induce spurious structures in the reconstructed flow, as noticed by Zauner *et al.* (2022), when investigating assimilation of sparse unsteady velocity in unsteady RANS models. In the present study, these spurious oscillations are also observed in the reconstructed mean velocity displayed in figure 2(g).

Interpolant-based nudging as proposed by Azouani *et al.* (2014) is a simple way to get a smoother forcing and reconstructed flow. In that case, the operator $\mathscr{I}$ can be defined as the product of two operators, i.e. $\mathscr{I}=\mathscr{M}\mathscr{L}$, where $\mathscr{L}$ is an interpolation of the measurement points in the measurement

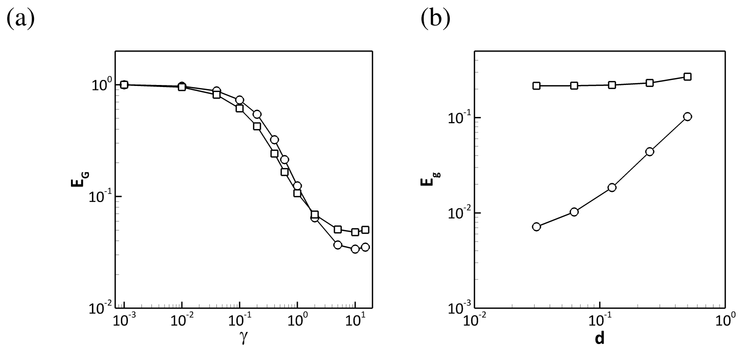

Figure 3: Evolution of the global velocity error E_g in (6) as a function of (a) the nudging coefficient γ (for $d = 0.5$) and (b) the measurement distance d (for $\gamma = 10$). Circle and square symbols respectively denote extrapolation and interpolation errors.

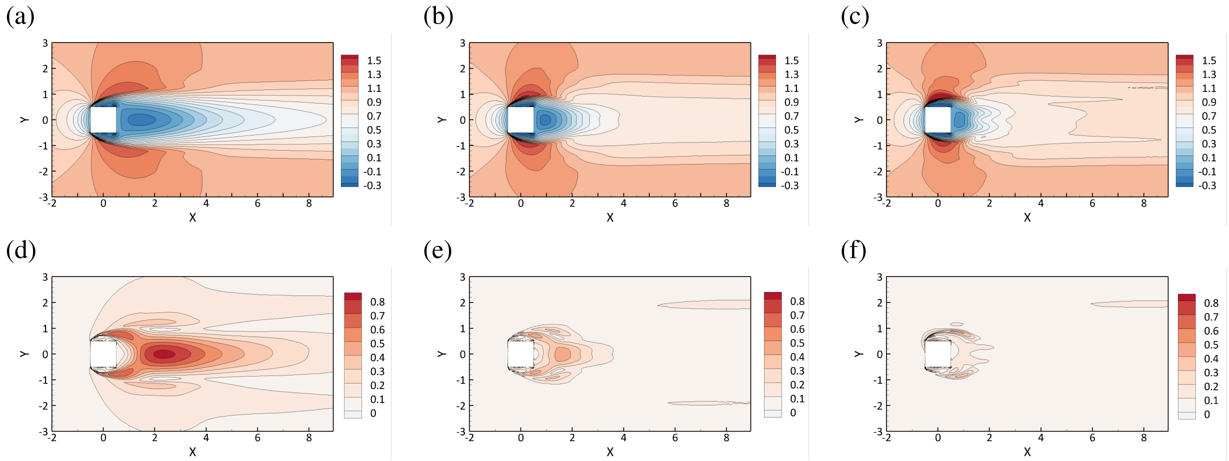

Figure 4: Effect of the nudging coefficient γ. (a-c) Streamwise velocity of the reconstructed field using equally-spaced measurements ($d = 0.5$) and (d-f) error velocity field to the reference (DNS) solution for (a,d) $\gamma = 0.1$, (b,e) $\gamma = 1$ and (c,f) $\gamma = 10$.

space and $\mathscr{M}$ performs a mapping from the measurement to the solution space, as detailed in the following. In the present study, these operators are defined after discretization of the governing equations with the finite element method described in the previous section. The measurement domain Ω_m is discretized using a Delaunay triangulation of the set of measurement points, as shown by the grid displayed in figure 2(b). This grid is symmetric with respect to the $y = 0$ axis so as to obtain a momentum forcing that satisfies the reflectional flow symmetry (see figure 2-e). Although we do not elaborate more on that point in the following, we still remark that satisfying this forcing symmetry is crucial to obtain accurate flow reconstruction, especially in case of very sparse data measurements. The linear interpolation of the data measurement is then obtained using the linear Lagrange finite element function defined on this mesh. For the streamwise reference velocity, it is defined as

$$\mathscr{L}u_r(\mathbf{x}) = \sum_{i=1}^{M} m_u^i \phi_u^i(\mathbf{x}), \tag{5}$$

where $\phi_u^i(\mathbf{x})$ are the Lagrange P1 elements defined on the measurement grid. Using the definition of Lagrange elements, we obtain that the interpolated function at measurement points is equal to the measurement data, i.e. $\mathscr{L}u_r(\mathbf{x}_j) = m_u^j$. Thanks to the operator $\mathscr{M}$, the forcing in the momentum equation is finally obtained by an interpolation of the velocity error from the measurement mesh to the solution mesh. More details can be found in appendix B in Zauner *et al.* (2022). The interest of the interpolant-based approach compared to the pointwise-based approach is clearly revealed when examining the interpolated function and forcing displayed in figures 2(b) and (e), respectively, that are now distributed in the measurement domain. This prevents from the appearance of spurious oscillations in the reconstructed solution, as shown in 2(h). A minor drawback of this approach is that, for errors of same magnitude, those located at the boundaries of the measurement domain tend to be larger than those located inside the measurement domain. This effect is simply due to the shape of the finite element functions $\phi_u^i(\mathbf{x})$ corresponding to boundary nodes i, that vanish non-smoothly out of the measurement domain. Since the forcing function is discontinuous at the boundaries of the measurement domain, the iso-contours of the reconstructed velocity exhibit abrupt spatial variations around the boundaries of the measurement domain. This is particularly visible in figure 2(e) at the top and bottom boundaries of the measurement domain. To suppress that effect, we propose to extend the boundaries of the measurement mesh by one layer in every direction, as shown in figure 2(c). The additional nodes located at the boundaries of this new mesh are ghost nodes where the interpolated solution vanishes, as shown in figure 2(c). Thus, they are not associated to new measurement data. They are rather added to obtain finite-element functions at the boundary nodes that smoothly vanish to zero. The new forcing function and reconstructed solution, shown in figure 2(f) and (i), respectively, are thus smoother around the boundaries of the measurement domain. When comparing the error distributions shown in figure 2(j,k,l) for the three approaches described above, we may conclude that the interpolant-based approaches provide a significant improvement of the velocity reconstruction inside the measurement domain by suppressing spurious oscillations related to the pointwise nature of the measurements. The one-layer extension of the measurement grid allows to further reduce the errors not only around the boundaries of the measurement domain but also further downstream. In the rest of the paper, we will focus on results obtained with that last approach.

We now examine the effect of the parameter γ on the accuracy of the flow reconstruction when using measurements that are equally spaced by the distance $d = 0.5$ in the domain Ω_m defined as $-1 \leq x \leq 4$ and $-1.5 \leq y \leq 1.5$. To that aim, we introduce the ratio of global velocity errors defined as

$$E_g = \left[\int_{\Omega_t} e(\mathbf{u}_\gamma)(\mathbf{x})^2 \right]^{\frac{1}{2}} / \left[\int_{\Omega_t} e(\mathbf{u})(\mathbf{x})^2 \right]^{\frac{1}{2}}, \qquad (6)$$

where $e(\mathbf{u}_\gamma)(\mathbf{x}) = \sqrt{(u_\gamma - u_r)^2 + (v_\gamma - v_r)^2}$ is the local error of the reconstructed velocity field $\mathbf{u}_\gamma = (u_\gamma, v_\gamma)$. The denominator corresponds to the error of the RANS solution. The spatial domain Ω_t can be the measurement domain Ω_m when investigating the interpolation error or defined as $-3 \leq x \leq 10$ and $-5 \leq y \leq 5$, when investigating the extrapolation error. Both errors are plotted in figure 3(a) as a function of the parameter γ, using circles for the interpolation error and squares for the extrapolation error. In both cases, a notable decrease of the error is observed for $\gamma > 0.01$ with a saturation observed for $\gamma \sim 10$. For large values of γ, the extrapolation error becomes slightly dominant, as observed in Zauner *et al.* (2022). The reconstructed velocity $\mathbf{u}(\gamma)$ and the distribution of the local error $e(\mathbf{u}_\gamma)$ are displayed in figure 4 for (a,d) $\gamma = 0.1$, (b,e) $\gamma = 1$ and (c,f) $\gamma = 10$. When increasing the value of γ, the size of the recirculation region clearly decreases and gets closer to that of the reference mean-flow. For $\gamma = 10$, the local error is below 0.1 everywhere in the wake of the cylinder. The largest value (around 0.4) is obtained around the shear layers existing at the top and bottom of the square cylinder. In these regions, the velocity gradients in the reference mean flow are strong and the linear-interpolation of measurements spaced by half a cylinder diameter ($d = 0.5$) is insufficient to improve the mean-flow estimation.

Looking at figure 3(b) showing the global interpolation and extrapolation errors as functions of d, decreasing the distance between measurements below $d = 0.5$ has only minor effect on the reconstructed flow velocity in the far wake. Therefore, we will focus on the near wake region of the square cylinder. Figure 5 displays (a,d,g) the interpolated measurements, (b,e,h) the reconstructed velocity and (c,f,i) the error field for measurement distances (a-c) $d = 0.5$, (d-f) $d = 0.25$, and (g-i) $d = 0.125$. The decrease of the error is significant for $d = 0.125$ and velocity gradients in the shear layers are now more accurately reconstructed. Local errors outside of the boundary layer drop well below 0.3, which is particularly evident in the near-wake region. The recirculation region delineated by the black curve in (h) approximates time-averaged DNS data reasonably well. The recirculation length extends up to $x = 1$, which is still slightly larger compared to the DNS result of 0.96. It may be worth noting that $d = 0.125$ remains a measurement resolution that is coarse compared to the flow structures close to the cylinder. In other words, measurements alone, even in this case, can clearly not fully characterize the flow, and interpolant-based nudging based on RANS here enables more accurate evaluation of high-gradient regions. Within the boundary layers, however, we still observe increased levels of velocity errors.

For separated flow configurations, unsteady RANS model can significantly improve the accuracy of the mean-flow estimation, as shown by Iaccarino *et al.* (2003). Indeed, the component of the Reynolds stress tensor induced by the low-frequency fluctuations strongly contributes to reduce the size of the mean flow recirculation. Recently, Zauner *et al.* (2022) performed the assimilation of unsteady pointwise velocity with the URANS model. Figure 6(b) show the streamwise velocity of the mean flow obtained with the unsteady data-assimilation of pointwise uniform measurements, distributed in the domain $-1.5 \leq x \leq 3$ and $-1.5 \leq y \leq 1.5$ with a spacing of $d = 1.5$. The results obtained using the present steady data-assimilation approach are shown in Figure 6(a). Despite a significant improvement of the mean-flow estimation obtained with RANS model, we should note that the nudged URANS simulations provide better results and refer to Zauner *et al.* (2022) for further discussion.

CONCLUSION

The present investigation of steady data assimilation suggests great potential using an interpolant-based nudging approach. Using sufficiently well-resolved velocity measurements, it can reduce errors near the cylinder by more than one order of magnitude, even if it is less accurate than the more-expensive unsteady nudging approach. The comparison of this highly-efficient data-assimilation method with variational data-assimilation approaches deserves further investigations, especially for turbulent flow configurations that do not exhibit low-frequency fluctuations, as the backward-facing step (Franceschini *et al.*, 2020) or the periodic hill (Volpiani *et al.*, 2021).

REFERENCES

Azouani, A., Olson, E. & Titi, E. S 2014 Continuous data assimilation using general interpolant observables. *Journal of Nonlinear Science* **24** (2), 277–304.

Brooks, A. N. & Hughes, T. J. R. 1982 Streamline upwind/Petrov-Galerkin formulations for convection dominated flows with particular emphasis on the incompressible Navier-Stokes equations. *Computer Methods in Applied Mechanics and Engineering* **32**, 199–259.

Dandois, J., Mary, I. & Brion, V. 2018 Large-eddy simulation of laminar transonic buffet. *Journal of Fluid Mechanics* **850**, 156–178.

Di Leoni, P. C., Mazzino, A. & Biferale, L. 2020 Synchronization to big data: Nudging the navier-stokes equations for data assimilation of turbulent flows. *Physical Review X* **10** (1), 011023.

Fabre, David, Citro, Vincenzo, Ferreira Sabino, D, Bonnefis, Paul, Sierra, Javier, Giannetti, Flavio & Pigou, Maxime 2018 A practical review on linear and nonlinear global approaches to flow instabilities. *Applied Mechanics Reviews* **70** (6).

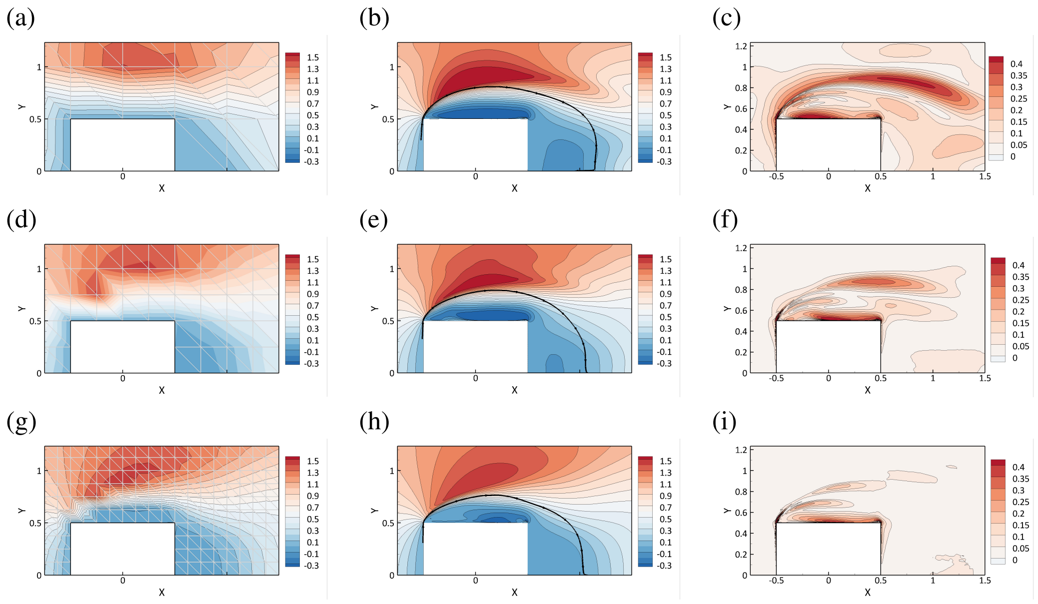

Figure 5: Reconstructed flow velocity around the upper side of the square cylinder for (a-c) $d = 0.5$, (d-f) $d = 0.25$ and (g-i) $d = 0.125$. Streamwise velocity of (a,d,g) the linearly interpolated measurement and (b,e,h) the reconstructed flow. (c,f,i) Error velocity fields. The coefficient is fixed to $\gamma = 10$. Grey lines in (a,d,g) show the measurement grid while the thick black curves in (b,e,h) delimit the recirculation regions.

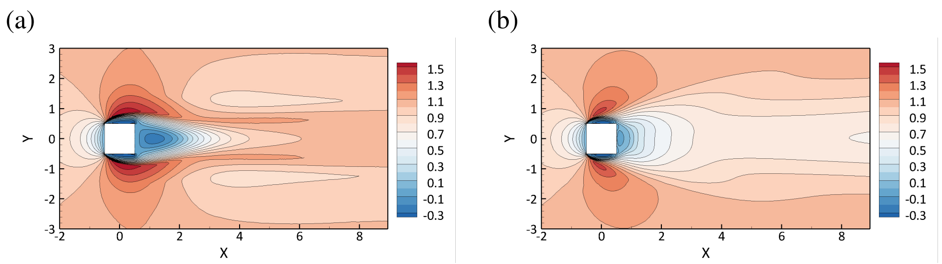

Figure 6: Comparison of mean-flow estimations obtained with (a,c) RANS and (b,d) URANS models. Streamwise velocity of the solution obtained (a,b) with standard models and (c,d) with assimilation of pointwise measurements spaced by the distance $d = 1.5$ in the domain $-1.5 \leq x \leq 3$ and $-1.5 \leq y \leq 1.5$.

Franceschini, Lucas, Sipp, Denis & Marquet, Olivier 2020 Mean-flow data assimilation based on minimal correction of turbulence models: Application to turbulent high reynolds number backward-facing step. *Phys. Rev. Fluids* **5**, 094603.

Hayase, T. 2015 Numerical simulation of real-world flows. *Fluid Dynamics Research* **47** (5), 051201.

Hecht, F. 2012 New development in FreeFem++. *Journal of Numerical Mathematics* **20**, 251–265.

Iaccarino, G., Ooi, A., Durbin, P. A. & Behnia, M. 2003 Reynolds averaged simulation of unsteady separated flow. *International Journal of Heat and Fluid Flow* **24** (2), 147–156.

Lakshmivarahan, S. & Lewis, J. M. 2013 Nudging methods: A critical overview. *Data Assimilation for Atmospheric, Oceanic and Hydrologic Applications (Vol. II)* pp. 27–57.

Mons, V., Chassaing, J.-C., Gomez, T. & Sagaut, P. 2016 Reconstruction of unsteady viscous flows using data assimilation schemes. *Journal of Computational Physics* **316**, 255–280.

Rebholz, L. G. & Zerfas, C. 2021 Simple and efficient continuous data assimilation of evolution equations via algebraic nudging. *Numerical Methods for Partial Differential Equations* **37** (3), 2588–2612.

Saredi, E., Ramesh, N. T., Sciacchitano, A. & Scarano, F. 2021 State observer data assimilation for rans with time-averaged 3d-piv data. *Computers & Fluids* **218**, 104827.

Spalart, P. R. & Allmaras, S. R. 1994 A one-equation turbulence model for aerodynamic flows. *La Recherche Aérospatiale* **1**, 5–21.

Volpiani, Pedro Stefanin, Meyer, Morten, Franceschini, Lucas, Dandois, Julien, Renac, Florent, Martin, Emeric, Marquet, Olivier & Sipp, Denis 2021 Machine learning-augmented turbulence modeling for rans simulations of massively separated flows. *Phys. Rev. Fluids* **6**, 064607.

Yegavian, R., Leclaire, B., Champagnat, F. & Marquet, O. 2015 Performance assessment of piv super-resolution with adjoint-based data assimilation. In *11th International symposium on particle image velocimetry, Santa Barbara, USA*, pp. 14–16.

Zauner, M., Mons, V., Marquet, O. & Leclaire, B. 2022 Nudging-based data assimilation of the turbulent flow around a square cylinder. *Journal of Fluid Mechanics* **937**.

Zerfas, C., Rebholz, L. G., Schneier, M. & Iliescu, T. 2019 Continuous data assimilation reduced order models of fluid flow. *Computer Methods in Applied Mechanics and Engineering* **357**, 112596.